

Calibrating baryonic feedback with weak lensing and fast radio bursts

Robert Reischke,^a Dennis Neumann,^a Klara Antonia Bertmann,^a
Steffen Hagstotz^{b,c} and Hendrik Hildebrandt^a

^aRuhr University Bochum, Faculty of Physics and Astronomy, Astronomical Institute (AIRUB), German Centre for Cosmological Lensing, 44780 Bochum, Germany

^bUniversitäts-Sternwarte, Fakultät für Physik, Ludwig-Maximilians Universität München, Scheinerstraße 1, D-81679 München, Germany

^cExcellence Cluster ORIGINS, Boltzmannstraße 2, D-85748 Garching, Germany

E-mail: reischke@posteo.net

Abstract. One of the key limitations of large-scale structure surveys of the current and future generation, such as Euclid, LSST-Rubin or Roman, is the influence of feedback processes on the distribution of matter in the Universe. This effect, called baryonic feedback, modifies the matter power spectrum on non-linear scales much stronger than any cosmological parameter of interest. Constraining these modifications is therefore key to unlock the full potential of the upcoming surveys, and we propose to do so with the help of Fast Radio Bursts (FRBs). FRBs are short, astrophysical radio transients of extragalactic origin. Their burst signal is dispersed by the free electrons in the large-scale-structure, leading to delayed arrival times at different frequencies characterised by the dispersion measure (DM). Since the dispersion measure is sensitive to the integrated line-of-sight electron density, it is a direct probe of the baryonic content of the Universe. We investigate how FRBs can break the degeneracies between cosmological and feedback parameters by correlating the observed Dispersion Measure with the weak gravitational lensing signal of a Euclid-like survey. In particular we use a simple one-parameter model controlling baryonic feedback, but we expect similar findings for more complex models. Within this model we find that $\sim 10^4$ FRBs are sufficient to constrain the baryonic feedback 10 times better than cosmic shear alone. Breaking this degeneracy will tighten the constraints considerably, for example we expect a factor of two improvement on the sum of neutrino masses.

Contents

1	Introduction	1
2	Large-Scale-Structure Probes	3
2.1	Cosmic Shear	3
2.2	FRB statistics	4
2.3	Power Spectra	6
2.4	Statistics	7
2.5	FRB redshifts	8
3	Results	10
3.1	Survey Specifications	10
3.2	Cosmological Constraints	12
4	Conclusion	14
A	Stability of the Fisher matrix	20
B	Effects of feedback on angular power spectra	20
C	Influence of redshift uncertainty on the inference	21
D	Noise increase due to redshift uncertainty	21

1 Introduction

Cosmic shear, the weak gravitational lensing effect imprinted on distant galaxies by the large-scale structure (LSS), is one of the primary science goals for the upcoming stage-4 surveys Euclid¹, Rubin-LSST² and the Roman telescope³. The foundations for these missions has been laid down by their predecessors: the Kilo-Degree Survey [1, 2, KiDS]⁴, the Dark Energy Survey [3, 4, DES]⁵ and the Subaru Hyper Suprime-Cam [5, 6, HSC]⁶.

The stage-4 surveys in particular target the highly non-linear regime of the matter distribution. Even though there is a wealth of information to be gathered at $k > 1 \text{ Mpc}^{-1}h$, baryonic feedback (BF) processes imprint large theoretical uncertainties on the total matter power spectrum. While the distribution of collisionless cold dark matter is well understood, at least on the level of numerical simulations, baryons remain the cause of large uncertainties. The displacement of baryons is due to nonlinear effects sourced by star formation, Supernovae, Active Galactic Nuclei (AGN) or cooling [see e.g. 7, 8, for reviews]. In turn, the displaced baryons affect the total matter power spectrum causing a reduction of power on intermediate scales due to outflows and energy injection by e.g. AGN, and an increase in power on small scales due to cooling. As these effects span a multitude of scales

¹<https://www.euclid-ec.org/>

²<https://www.lsst.org/>

³<https://roman.gsfc.nasa.gov/>

⁴<https://kids.strw.leidenuniv.nl/>

⁵<https://www.darkenergysurvey.org/>

⁶<https://hsc.mtk.nao.ac.jp/ssp/>

and are highly non-linear, they are almost impossible to model analytically and are thus extracted from hydrodynamical simulations which include a model with a fixed set of parameters to control the feedback strength. The main challenge arises from the fact that feedback processes originate from physics, which is far below the resolution of the numerical simulation. Each simulation therefore has sub-grid models implemented. However, different models can lead to significantly different predictions for the matter clustering statistics at small scales [9, 10]. For example, in the CAMELS simulation suite [11], two very distinct sub-grid models are implemented. However, the differences are largely due to higher gas temperature in the inter-galactic medium [11]. Another suite of simulations are the BAHAMAS simulations [12] whose power spectra have been calibrated to a hydrodynamical version of the halo model [13], specifically designed for weak lensing cross-correlation studies with the thermal Sunyaev-Zel'dovich (tSZ) effect [14] caused by the thermal velocity of hot electrons in galaxy clusters.

Any independent measurement of the baryon distribution can help to independently constrain feedback models. It was shown in [14] that e.g. the tSZ effect has the potential to partially calibrate the feedback strength and breaking degeneracies (see also a discussion [15]). Another related possibility to measure the electron distribution uses not thermal, but the bulk velocities of galaxy clusters for the kinetic SZ (kSZ) effect [16, 17]. This was done by various studies using data from the Atacama Cosmology Telescope [18, 19], from Planck [20] and SPT [21] and can also break degeneracies between feedback models [22, 23]. These measurements start to be able to discriminate between different feedback models. It was for example shown in [24] prefer stronger feedback which was supported recently as well by [25]. At the moment, the tSZ and kSZ effect are the major way to measure the electron distribution in the Universe. It is therefore important to add additional probes for (i) more constraining power and (ii) different systematic effects in the measurements.

An alternative probe of the electron distribution are fast radio bursts (FRBs). FRBs are short transients, lasting typically a few milliseconds, with frequencies ranging from ~ 100 MHz to several GHz. Since the radio signal is travelling through the ionized intergalactic medium (IGM), each frequency of the pulse experiences a delay characterised by the dispersion measure (DM) proportional to the integrated free electron density along the line-of-sight [e.g. 26–30]. The mechanism responsible for the radio emission is currently unknown, but the isotropic occurrence of the events detected so far shows no alignment with the Milky Way disk and the measured DM for most events is very large, requiring an extragalactic origin. By now, a subset of events has been localised to galaxies up to redshifts $z \sim 1$. In general, the total DM associated with an extragalactic FRB event consists of contributions from the host galaxy, the Milky Way and the diffuse electrons in the large-scale structure (LSS). Several authors, therefore, proposed to use the DM inferred from FRBs as a cosmological probe using either the averaged signal [e.g. 31–38] or the statistics of DM fluctuations [e.g. 39–45].

Currently, roughly ~ 1000 FRBs are detected, but estimated rates of ~ 1000 events/night/sky allow surveys such as CHIME, UTMOST, HIRAX, ASKAP, CHORD, DSA-2000 or SKA [46, 47, 47–51] to provide at least $\sim 10^4$ FRBs per decade. Although FRBs do not show spectral features that allow for accurate redshift estimation, the accumulated DM can be translated into a noisy distance estimate [39]. Since FRBs are observed with $DM \geq 1000 \text{ pc cm}^{-3}$ and models of the Milky Way suggest $DM \leq 50 \text{ pc cm}^{-3}$ due to gas in our Galaxy for most directions on the sky [52], the majority of the DM signal originates from the diffuse electrons in the IGM, which follows the total matter distribution on large scales. Although the host galaxy contribution is still under debate, its magnitude is expected to be comparable to that of the Milky Way and hence usually smaller than the contribution from the LSS. While the host dispersion can reach several hundreds pc cm^{-3} in rare cases, particularly when the FRB originates in the trailing edge of the host galaxy (as seen by the observer), one typically finds that $DM_{\text{LSS}} > DM_{\text{host}}$ for FRBs at redshifts $z \sim 1$. The dispersion of

FRBs tests, similar to cosmic shear, an integrated quantity along the line-of-sight. However, since host galaxies typically contribute less to the DM than the LSS, FRBs are way less affected by shot noise compared to cosmic shear. Combining FRBs and cosmic shear will accordingly probe similar structures, but testing the baryon distribution and the total matter distribution respectively, enabling strong constraints on the different clustering behaviour of both components. It should be noted that the cosmic shear signal has a vanishing expectation value, unlike the DM of FRBs. However, since we are interested in the statistical properties of the DM, this is not that important for our study here.

In this paper, we will hence investigate the potential gains from combining a stage-4 cosmic shear measurement with the statistical properties of the DM measured from an FRB sample, which should be available on the same timescale as cosmic shear data from Euclid and Rubin-LSST. To this end, we simulate mock data for these kinds of surveys and carry out a Fisher and MCMC analysis to investigate the impact of adding FRBs in a cosmological analysis with a particular focus on the baryonic feedback and on the cosmological parameters that are most affected by feedback uncertainties, such as the sum of neutrino masses. The paper is structured as follows: In Section 2, we summarise the LSS structure probes and describe the methodology for our analysis. Section 3 is devoted to the discussion of the results and a comparison with other probes of the electron distribution. Lastly, we conclude in Section 4 and discuss potential ways forward.

2 Large-Scale-Structure Probes

In this section, we summarise the two probes used to test the matter distribution: cosmic shear and FRB dispersion measure. We introduce cosmic shear in Section 2.1 and DM correlations in Section 2.2, which are sensitive to the full matter and electron distribution respectively and can hence be used to break degeneracies between baryonic feedback and cosmological parameters.

2.1 Cosmic Shear

Cosmic shear is the gravitational lensing effect of the LSS on an ensemble of background sources (galaxies) and is thus sensitive to the projected matter distribution along the line-of-sight. The cosmological information of gravitational lensing by the LSS is contained in the traceless part of the cosmic shear tensor:

$$\gamma_i = 2 \int d\chi W_{\gamma_i}(\chi) \delta\delta\Phi(\hat{\mathbf{x}}, \chi), \quad (2.1)$$

in absence of anisotropic stress. Here γ_i denotes the shear in the i -th tomographic bin, W_{γ_i} is a geometrical weighting function defined below, Φ are the scalar metric perturbations, χ the co-moving distance and δ is the *eth*-derivative for a spin-2 field. Using Poisson's equation, one can relate the metric perturbations to the density contrast, yielding the following expression for the angular power spectrum:

$$C_\ell^{\gamma_i\gamma_j} = \frac{(\ell+2)!}{(\ell-2)!} \frac{2}{\pi} \int d\chi_1 \int d\chi_2 \int k^2 dk K_i(\chi_1) K_j(\chi_2) \frac{j_\ell(\chi_1 k)}{(k\chi_1)^2} \frac{j_\ell(\chi_2 k)}{(k\chi_2)^2} \sqrt{P_\delta(k, \chi_1) P_\delta(k, \chi_2)}. \quad (2.2)$$

Approximating the Bessel function by a Dirac distribution [53, 54], the integrations over $\chi_{1,2}$ can be carried out to find the commonly used expression for the angular power spectrum:

$$C_\ell^{\gamma_i\gamma_j} = \int_0^{\chi_H} \frac{d\chi}{\chi^2} W_\gamma^{(i)}(\chi) W_\gamma^{(j)}(\chi) P_\delta\left(\frac{\ell+1/2}{\chi}, \chi\right), \quad (2.3)$$

Survey	area f_{sky}	number of sources	intrinsic noise σ	tomographic bins
FRB	0.7	10^4	50 pc cm^{-3}	1
Euclid	0.3	30 arcmin^{-2}	0.212	10
KiDS	0.025	7.55 arcmin^{-2}	0.28	5

Table 1. Survey settings assumed in the analysis. The number of sources for the cosmic shear surveys is an average density over all tomographic bins. The actual number in each tomographic bin can be slightly different. The same holds for the ellipticity dispersion, for more details see [57] and [58]. Note that we give the ellipticity dispersion of a single component for cosmic shear and that the intrinsic noise is the averaged noise over the whole FRB sample.

which will be accurate enough for cosmic shear even for the next generation of surveys [55] due to the broad lensing kernel. Here P_δ is the matter power spectrum, for which we use the emulated spectrum from HMcode[56]. $W_\gamma^{(i)}(\chi)$ is the lensing weight of the i -th tomographic bin as given by:

$$W_\gamma^{(i)}(\chi) = \frac{3\Omega_{\text{m}0}}{2\chi_{\text{H}}^2} \frac{\chi}{a(\chi)} \int_\chi^{\chi_{\text{H}}} d\chi' n_s^{(i)}(\chi') \frac{\chi' - \chi}{\chi'} . \quad (2.4)$$

Here a is the scale factor, $\Omega_{\text{m}0}$ the matter density parameter today, χ_{H} the Hubble radius and $n_s^{(i)}$ is the distribution of sources.

Lastly, due to the finite number of background galaxies, observed spectra obtain a shape-noise contribution:

$$C_\ell^{\gamma_i \gamma_j} \rightarrow C_\ell^{\gamma_i \gamma_j} + \frac{\sigma_{\epsilon,i}^2}{2\bar{n}_i} \delta_{ij}^{\text{K}} , \quad (2.5)$$

with the total ellipticity dispersion $\sigma_{\epsilon,i}^2$ and the average number of sources \bar{n}_i in the i -th tomographic bin. δ_{ij}^{K} is the Kronecker delta, and ensures that the intrinsic shapes of different redshift bins are uncorrelated.

2.2 FRB statistics

FRB pulses undergo dispersion while travelling through the ionized IGM, causing a frequency-dependent (proportional to ν^{-2}) offset of arrival times. The corresponding time delay measured $\delta t(\hat{\mathbf{x}}, z)$ for an FRB at redshift z in direction $\hat{\mathbf{x}}$ proportional to the observed dispersion measure: $\delta t(\hat{\mathbf{x}}, z) = \text{DM}_{\text{tot}}(\hat{\mathbf{x}}, z)\nu^{-2}$. The observed DM can be broken up into different components:

$$\text{DM}_{\text{tot}}(\hat{\mathbf{x}}, z) = \text{DM}_{\text{LSS}}(\hat{\mathbf{x}}, z) + \text{DM}_{\text{MW}}(\hat{\mathbf{x}}) + \text{DM}_{\text{host}}(z) , \quad (2.6)$$

where $\text{DM}_{\text{LSS}}(\hat{\mathbf{x}}, z)$ is the DM caused by the electron distribution in the LSS, while $\text{DM}_{\text{MW}}(\hat{\mathbf{x}})$ and $\text{DM}_{\text{host}}(z)$ describe the contributions from the Milky Way and the host galaxy, respectively. Here we made the dependence on redshift and direction explicit. Note that the rest-frame DM of the host, $\text{DM}_{\text{host,rf}}$, is observed as $\text{DM}_{\text{host}}(z) = (1+z)^{-1} \text{DM}_{\text{host,rf}}$.

Current models of the galactic electron distribution predict $\text{DM}_{\text{MW}} \sim 60 \text{ pc cm}^{-3}$ over most of the sky [52, 59]. Since the galactic electron distribution also depends on the direction $\hat{\mathbf{x}}$, it is in principle a large contaminant for DM correlation measurement. Here, however, we assume that it can be modelled accurately enough to be subtracted from the observed DM without leaving a significant imprint on the measured DM correlations. Naively, one can expect $\text{DM}_{\text{host}}(z)$ to be very similar to DM_{MW} . However, in practice it depends strongly on the host galaxy's properties and is thus treated

as a free parameter. Since it does not correlate with the LSS, it will not leave an imprint on the DM correlation but rather act as a noise term, as we will discuss later. Finally, the LSS contribution to the DM is given by [44]

$$\text{DM}_{\text{LSS}}(\hat{\mathbf{x}}, z) = \chi_{\text{H}} \int_0^z dz' n_e(\mathbf{x}, z') \frac{1+z'}{E(z')}, \quad (2.7)$$

where $E(z)$ is the expansion function and n_e the electron density which depends on the local matter over-density, $\delta_{\text{m}}(\mathbf{x}, z)$ and the electron bias $b_e(\mathbf{x}, z)$:

$$n_e(\mathbf{x}, z) = \frac{\bar{\rho}_{\text{b}}(z)}{m_{\text{p}}} F(z) [1 + b_e(\mathbf{x}, z) \delta_{\text{m}}(\mathbf{x}, z)]. \quad (2.8)$$

Here we used the mean baryon density $\bar{\rho}_{\text{b}}(z)$, the proton mass m_{p} and the mass fraction $F(z)$ of electrons in the IGM. The latter can be expressed as:

$$F(z) = f_{\text{IGM}}(z) [Y_{\text{H}} X_{\text{e,H}}(z) + Y_{\text{He}} X_{\text{e,He}}(z)], \quad (2.9)$$

with the mass fraction of hydrogen and helium $Y_{\text{H}} = 0.75$ and $Y_{\text{He}} = 0.25$ respectively, as well as their ionization fractions $X_{\text{e,H}}(z)$ and $X_{\text{e,He}}(z)$. Since both hydrogen and helium are both fully ionised for $z \lesssim 3$ [60, 61] we set $X_{\text{e,H}} = X_{\text{e,He}} = 1$. It should be noted that for the survey settings considered here, the majority of the signal arises from $z < 3$, so the last assumption is indeed well justified. The fraction of baryons in the IGM, $f_{\text{IGM}}(z)$, has a slight redshift dependence [62], with 10% (20%) locked up in galaxies at $z \gtrsim 1.5$ ($\lesssim 0.4$). Rewriting eq. (2.7) leaves us with the following expression:

$$\text{DM}_{\text{LSS}}(\hat{\mathbf{x}}, z) = \mathcal{A} \int_0^z dz' \frac{1+z'}{E(z')} F(z') [1 + b_e(\mathbf{x}, z') \delta_{\text{m}}(\mathbf{x}, z')], \quad (2.10)$$

with the amplitude

$$\mathcal{A} \equiv \frac{3H_0^2 \Omega_{\text{b}0} \chi_{\text{H}}}{8\pi G m_{\text{p}}}. \quad (2.11)$$

A very intriguing aspect of FRBs is that the cosmological contribution is typically larger than the contribution from the host or the Milky Way. This is in large contrast to cosmic shear, where the ellipticity imprinted by gravitational lensing is a percent effect of the intrinsic ellipticity. Therefore, far fewer FRBs are required for a significant detection of DM correlations compared the number of galaxies in weak lensing studies. Following [44], we rewrite the LSS contribution to the DM as a background contribution and a perturbation:

$$\text{DM}_{\text{LSS}}(\hat{\mathbf{x}}, z) = \langle \text{DM}_{\text{LSS}} \rangle(z) + \mathcal{D}(\hat{\mathbf{x}}, z), \quad (2.12)$$

where $\mathcal{D}(\hat{\mathbf{x}}, z)$ is the effective DM induced by the fluctuations in the LSS. In full analogy to cosmic shear, we assume a source-redshift distribution $n_{\text{FRB}}(z)$. To be accurate, one is using a source-DM distribution, which in turn is converted to $n_{\text{FRB}}(z(\text{DM}))$. This procedure was discussed in [44] and [63]. Note that we do not make use of the fraction of FRBs that will most likely have an identified host with redshift estimates, which additionally improves the expected constraints. By rearranging integration limits one finds

$$\mathcal{D}(\hat{\mathbf{x}}) = \int_0^{\chi_{\text{H}}} d\chi W_{\mathcal{D}}(\chi) \delta_{\text{e}}(\hat{\mathbf{x}}, z(\chi)), \quad (2.13)$$

with the averaged weighting function

$$W_{\mathcal{D}}(\chi) = W(\chi) \int_{\chi}^{\chi_{\text{H}}} d\chi' n_{\text{FRB}}(\chi'), \quad (2.14)$$

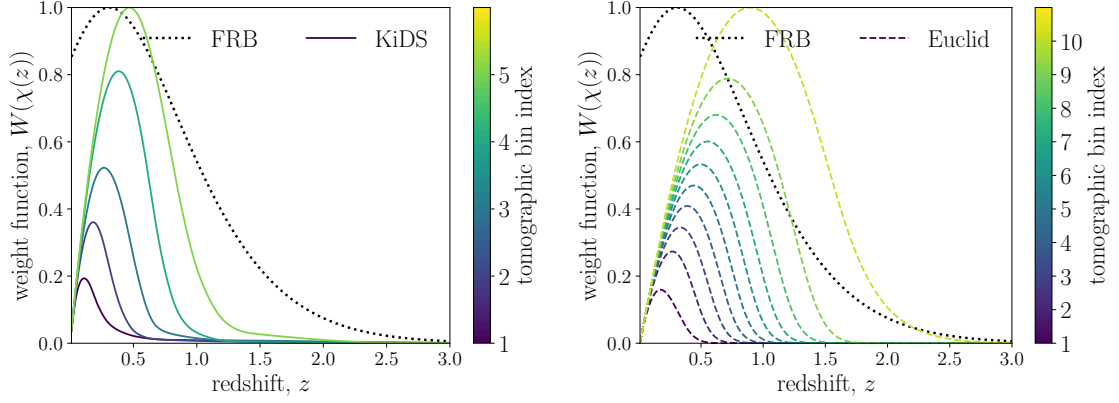


Figure 1. Weighting function for FRBs (dotted black line) and for cosmic shear with the KiDS redshift distribution (left plot) or Euclid’s redshift distribution (right plot). The colour bar shows the tomographic bin index. All weighting functions have been normalised to the peak value. In the case of cosmic shear, the peak of the last tomographic bin was used.

and $W(\chi)$ being defined via eq. (D.3):

$$W(\chi) = \mathcal{A} \frac{F(z(\chi))(1 + z(\chi))}{E(z(\chi))} \left| \frac{dz}{d\chi} \right|. \quad (2.15)$$

In complete analogy to cosmic shear, the angular power spectrum for the DM fluctuations \mathcal{D} is given by:

$$C^{\mathcal{D}\mathcal{D}}(\ell) = \frac{2}{\pi} \int d\chi_1 \int d\chi_2 \int k^2 dk W_{\mathcal{D}}(\chi_1) W_{\mathcal{D}}(\chi_2) \sqrt{P_{ee}(k, \chi_1) P_{ee}(k, \chi_2)} j_\ell(k\chi_1) j_\ell(k\chi_2). \quad (2.16)$$

As discussed in [44], the Limber approximation is suitable for DM correlations as well. Hence, we again use eq. (2.3). When cross-correlating cosmic shear and the DM, we replace one of the weight functions in Equation (2.3) with $W_{\mathcal{D}}$ and the matter power spectrum by the electron-matter cross power spectrum $P_{\delta e}$.

Lastly, the host galaxy contribution acts as a shot noise contribution with variance σ_{host}^2 per event, thus adding a white noise contribution to the observed spectra:

$$C^{\mathcal{D}\mathcal{D}}(\ell) \rightarrow C^{\mathcal{D}\mathcal{D}}(\ell) + \frac{\sigma_{\text{host}}^2}{\bar{n}}, \quad (2.17)$$

here σ_{host}^2 should be seen as the effective host of the FRB sample

$$\sigma_{\text{host}}^2 = \int dz n_{\text{FRB}}(z) \frac{\sigma_{\text{host},0}^2}{(1+z)^2}. \quad (2.18)$$

2.3 Power Spectra

The angular power spectra in Equation (2.2) and Equation (2.16) are integrals over the matter power spectrum and the electron power spectrum. Cross-correlating the probes also requires the matter-electron power spectrum. We use `pyhmcode` [13, 14, 56] which was fitted to the `BAHAMAS` [12] and

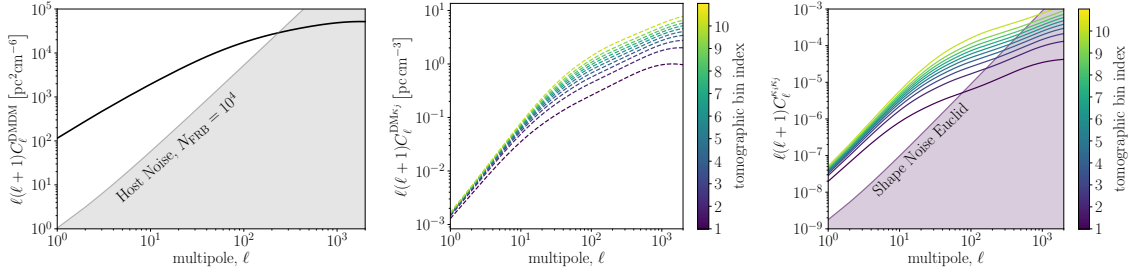


Figure 2. Angular power spectra for the Euclid redshift distributions and an FRB sample with $\alpha = 3.5$ as defined in Equation (3.1). Note that all three plots have different units. The noise levels are, however, consistently scaled so that they represent the true noise level in each analysis. **Left:** The solid black line shows the auto-correlation spectrum of the DM. The shaded area indicates the DM noise originating from the scatter in the host contribution. **Centre:** The dashed coloured lines show the cross-power spectra between the DM and the lensing convergence κ_i in each of the ten tomographic Euclid redshift bins. The noise contribution for the cross-correlation vanishes. **Right:** Auto-correlation, $i = j$, angular power spectra for the ten Euclid tomographic bins. The shaded region again quantifies the noise-level for Euclid cosmic shear.

COSMO-OWLS [64] simulation suites to reproduce the power spectra of matter, gas, stars and pressure assuming a halo model. The baryonic feedback in `pyhmcode` is controlled by a single parameter, the strength of AGN encapsulated in T_{AGN} . This AGN temperature should just be seen as a nuisance parameter without physical correspondence in the real Universe. Larger AGN temperatures lead to different suppression on large k (and rise again on even smaller scales). For current cosmological surveys, this description is usually flexible enough, since more extended models are likely to be prior dominated and therefore offer too much flexibility. For future surveys, however, more flexible emulators might be needed [65–67], allowing for more freedom at non-linear scales due to baryonic feedback.

2.4 Statistics

Full sky surveys measure $2\ell + 1$ independent modes per multipole ℓ . For any projected fields $f_i(\hat{\mathbf{x}})$, one would derive modes $f_{i,\ell m}$ from a spherical harmonic decomposition. Assuming that the likelihood for the set of modes $\{f_{i,\ell m}\}$ is a multivariate Gaussian with zero mean and covariance (or 2-point correlation) \mathbf{C} with components

$$(\mathbf{C}_\ell)_{ij} = \langle f_{i,\ell m} f_{j,\ell' m'}^* \rangle \equiv \delta_{mm'}^{\mathbf{K}} \delta_{\ell\ell'}^{\mathbf{K}} C_\ell^{f_i f_j}, \quad (2.19)$$

the Fisher matrix is given by [68]:

$$F_{\alpha\beta} = f_{\text{sky}} \sum_{\ell} \frac{2\ell + 1}{2} \text{tr} \left(\mathbf{C}_\ell^{-1} \partial_\alpha \mathbf{C}_\ell \mathbf{C}_\ell^{-1} \partial_\beta \mathbf{C}_\ell \right). \quad (2.20)$$

Here Greek indices label parameters, and the observed sky fraction f_{sky} accounts for incomplete sky coverage. The inverse of the Fisher matrix \mathbf{F}^{-1} yields the covariance matrix of the parameters and serves as a lower limit for obtainable errors given the survey settings by means of the Cramér-Rao bound.

Since the derivative in eq. (2.20) is calculated numerically, small difference can propagate into the matrix inversion to obtain possible constraints. Therefore, we check the stability of the derivative in appendix A. Lastly, we are also calculating the signal-to-noise ratio (SNR) of the measurement,

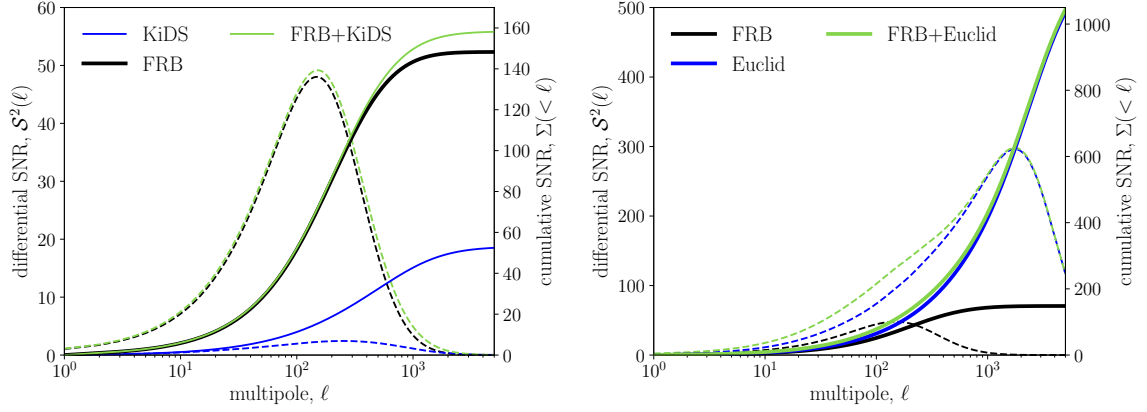


Figure 3. Signal-to-Noise ratio (SNR) for a joint analysis of a cosmic shear survey with DM statistics. Dashed lines depict the squared SNR at each multipole, while solid lines show the cumulative SNR below the indicated multipole, ℓ (compare to Equation 2.21). **Left:** for KiDS, **Right:** for Euclid. Note that the same FRB sample was considered in both cases. The number of FRBs in this analysis is 10^4 .

i.e. we assume that one wants to measure the amplitude, A , of the cosmological term in eqs. (2.5) and (2.17). Using eq. (2.20) for $\mathbf{C} = \mathbf{A}\mathbf{S} + \mathbf{N}$, one finds

$$\Sigma^2(\leq \ell) = f_{\text{sky}} \sum_{\ell'}^{\ell} \frac{2\ell' + 1}{2} \text{tr}(\mathbf{C}_{\ell'}^{-1} \mathbf{S}_{\ell'} \mathbf{C}_{\ell'}^{-1} \mathbf{S}_{\ell'}) \equiv \sum_{\ell'}^{\ell} \mathcal{S}^2(\ell'). \quad (2.21)$$

In the case here, the covariance takes the form:

$$\mathbf{C}_{\ell} = \begin{pmatrix} \mathbf{C}_{\ell}^{\mathcal{D}\mathcal{D}} & \mathbf{C}_{\ell}^{\mathcal{D}\gamma} \\ \mathbf{C}_{\ell}^{\gamma\mathcal{D}} & \mathbf{C}_{\ell}^{\gamma\gamma} \end{pmatrix}. \quad (2.22)$$

Note that noise between the DM and the shear are uncorrelated, hence $\mathbf{C}_{\ell}^{\gamma\mathcal{D}}$ does not have a flat noise contribution. Lastly, Equation (2.20), assumes that all probes are measured over the same footprint f_{sky} . In order to account for different footprints we modify the Fisher matrix as follows:

$$\mathbf{F}^{\text{FRB+lensing}} \rightarrow f_{\text{sky,min}} \mathbf{F}^{\text{FRB+lensing}} + (f_{\text{sky,max}} - f_{\text{sky,min}}) \mathbf{F}_{\text{max}}^{\text{FRB/lensing}} \quad (2.23)$$

where $f_{\text{sky,min}}$ and $f_{\text{sky,max}}$ identify the small and larger footprint of the two surveys respectively and $\mathbf{F}_{\text{max}}^{\text{FRB/lensing}}$ is the corresponding Fisher matrix of the larger footprint. This replacement assumes that the footprints of from which the angular power spectra are estimated overlap completely, making it equivalent to studying the power spectra estimators with a purely Gaussian covariance.

2.5 FRB redshifts

Before moving to the cosmological results, we want to review the issue of the host identification with FRBs and the limitations of this study. Suppose an FRB is observed at position $\hat{\mathbf{x}}$ without host identification with measured $\text{DM}_{\text{tot}}(\hat{\mathbf{x}})$, where we neglected the redshift dependence purposefully as it is not known *a priori*. However, in principle, we can always invert the homogeneous DM- z relation to obtain a noisy estimate of the redshift

$$\hat{z} \sim p_{\hat{z}}(z|\text{DM}_{\text{tot}}(\hat{\mathbf{x}})), \quad (2.24)$$

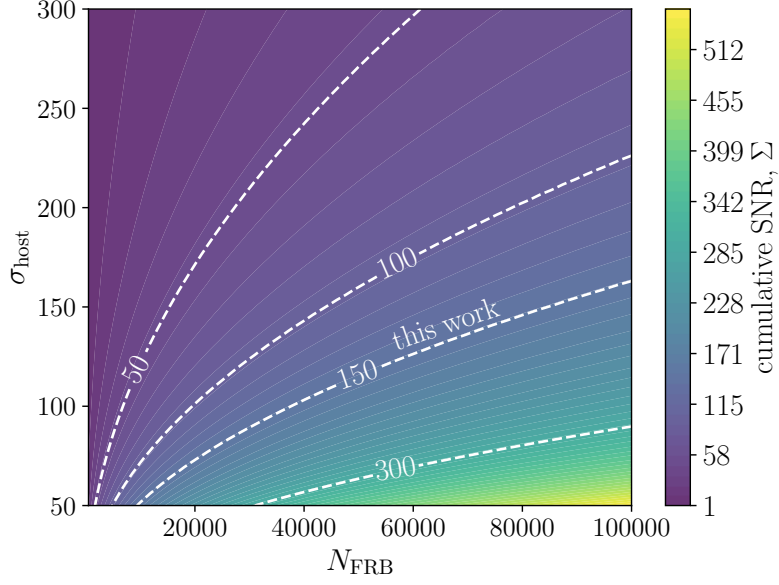


Figure 4. Cumulative SNR as a function of the Noise specification in Equation (2.17), where $\bar{n} = N_{\text{FRB}}/(4\pi)$. White lines indicate selected curves of constant SNR.

where we estimate \hat{z} such that

$$\hat{z} = z(\langle \text{DM}_{\text{LSS}} \rangle) = z(\text{DM}_{\text{tot}}(\hat{\mathbf{x}}) - \langle \text{DM}_{\text{host}} \rangle - \text{DM}_{\text{MW}}(\hat{\mathbf{x}})). \quad (2.25)$$

As in [44], the redshift distribution, $n(z)$, is essentially given by marginalising over the all possible observed DM:

$$n(z) = \int d\hat{z} \, n(\hat{z}) p_{\hat{z}}(z | \text{DM}_{\text{tot}}). \quad (2.26)$$

This would then enter the expression for the power spectrum and as long as the redshift scatter is not large compared to the full redshift range of the FRB sample, this will not seriously degrade the results. Additionally, we assume here that there is already a galaxy sample with calibrated redshifts calibrated in this analysis present, namely the source sample used for cosmic shear. Due to the inclusion of the DM-shear cross-correlation, the $n_{\text{FRB}}(z)$, see Equation (3.1), can be self-calibrated. We test this by assuming that we have an initial guess for the redshift distribution of the FRBs by means of Equation (2.25) and that the residual noise can be described by shifting the mean of the redshift distribution by some value δz which is known to be sufficient for integrated effects such as cosmic shear or the DM [69]

$$n_{\text{FRB}}(z) \mapsto n_{\text{FRB}}(z + \delta z). \quad (2.27)$$

The results of this exercise are presented in Appendix C, where we demonstrate that this effect is indeed small for the case considered here. The general case of calibrating the redshift distribution of FRBs when only a subset of the observed events has known hosts is more complicated. For a first estimation of this effect we refer to Appendix D. However, in the future we intend to do this more rigorously, by fitting both the homogeneous component of the DM as well as its statistical properties at the same time.

3 Results

3.1 Survey Specifications

The survey specifications are given in Table 1 and the following redshift distribution for the FRBs is assumed

$$n_{\text{FRB}}(z) \propto z^2 e^{-z\alpha}, \quad (3.1)$$

where $\alpha = 3.5$ controls the depth of the survey. For the weak lensing surveys, the redshift distributions are discussed in [57] and [70]. We show the weighting functions $W(\chi)$ for the individual surveys in Figure 1. The number of FRBs used to estimate the correlation is 10^4 , which is well in reach of SKA or DSA-2000 [50] being currently build and aiming for $> 10^4$ FRBs with localisation. The colour bar in Figure 1 indicates the tomographic bin index for the weak lensing surveys. All weights are normalised to the maximum of the respective highest redshift bin. There is substantial overlap with Euclid (apart from the last tomographic bin) and complete overlap with a survey such as KiDS.

Figure 2 shows the three types of angular power spectra used in this analysis. On the left side, the DM-auto-correlation angular power spectrum is shown in black. Furthermore we indicate the intrinsic noise properties of this measurement by the grey shaded area as calculated in Equation (2.17). From the figure it is clear that the DM correlations dominate the intrinsic fluctuations due to the host contribution up to $\ell \sim 100$. Above this multipole the host noise takes and washes out the cosmologically interesting signal. In the centre of Figure 2, we show the cross-power angular power spectrum between the DM and each of the ten tomographic cosmic shear power spectra as they will be measured by Euclid. Note that, since cosmic shear is dimensionless, the units of the spectra changed. In this case, there is no shaded area as the cross-spectra are noise-free. One can see that the curves are less flat at higher ℓ since the pure electron power spectrum is much more suppressed than the cross-power spectrum between matter and baryons at small scales. Lastly, we show the dimensionless cosmic shear angular power spectrum in the right panel. For more visibility only the tomographic auto-correlation, $i = j$, are shown. Here the steepness at larger ℓ is even more visible, again a result of fewer baryonic suppression of the total matter power spectrum compared to the electron power spectrum. The shaded area indicates the noise level of Euclid which is the same in all tomographic bins as they are equi-populated and have the same intrinsic ellipticity dispersion, σ_e .

Before discussing the potential SNR of the measurement we would like to stress an important point. In Figure 2, the spectra have different dimensionality, since the corresponding fields have different dimensions themselves. Therefore one should not compare the amplitude between the different C_{ell} directly. What is, however, important is the relative amplitude of each C_ℓ relative to the noise contribution as they define the relative signal strength. As long as this is done consistently, it does not matter if one investigates relative fluctuations as in the case of the cosmic shear, or dimensionful fluctuations as for the DM. In this sense, the modes of the fields carry the correct statistical information irrespective of the chosen unit system if their covariance is specified consistently. This is done by specifying the C_ℓ in Equation (2.22) at each multipole, ℓ . This approach is completely equivalent to taking the estimated angular power spectrum as the model and concatenate them into a large data vector with Gaussian covariance. Also here, entry in the data vector can have arbitrary and different units as long as this is reflected in the covariance as well. Since the pure noise contributions have the same dimensions as the C_ℓ this is taken into account properly in the present case. Therefore we conclude, while comparing the power spectra directly to each other is not meaningful in any way, their SNR curves as shown in Figure 3 as a function of multipole ℓ are invariant under linear transformations (as unit transformations are always are). Dashed lines in Figure 3 illustrate the squared differential SNR at each multipole, while solid lines show the integrated SNR. In the case of a stage-3

Probe	h	Ω_{cdm}	σ_8	Ω_b	w_0	w_1	$\log_{10} T_{\text{AGN}}$	$\sum m_{\text{v}} [\text{eV}]$	n_s
Fisher									
Euclid	0.1	0.019	0.039	0.015	0.215	0.908	0.208	0.334	0.092
KiDS	0.678	0.026	0.08	0.117	-	-	1.145	-	-
FRB	1.483	1.471	0.958	0.128	9.955	53.246	1.219	2.559	2.018
Euclid+FRB	0.064 (85 %)	0.014 (45 %)	0.022 (95 %)	0.006 (679 %)	0.17 (47 %)	0.677 (57 %)	0.014 (2153 %)	0.191 (122 %)	0.037 (340 %)
KiDS+FRB	0.041	0.026	0.05	0.006	-	-	1.145	-	-
MCMC									
Prior	[0.64, 0.82]	[0.051, 0.255] h^{-2}	[0.7, 1.2]	[0.019, 0.026] h^{-2}	[-1, 0]	[-1 - w_0 , - w_0]	none	[0, ∞]	none
Euclid	0.113	0.01	0.016	0.013	0.101	0.237	0.196	0.137	0.117
Euclid + FRB	0.065 (73 %)	0.009 (5 %)	0.012 (26 %)	0.005 (172 %)	0.092 (10 %)	0.21 (12 %)	0.017 (1020 %)	0.089 (54 %)	0.051 (129 %)

Table 2. One dimensional marginal constraints for 68 % confidence on the cosmological and feedback parameters using different survey settings. The first part of the table uses a Fisher analysis with no prior. In the lower part we fit a noiseless data vector with using MCMC and flat priors on some of the parameters. For the case of Euclid+FRB, we also quote the relative reduction of error in percent. Note that the FRB case is only given for the full parameter set and uses 10^4 FRBs.

survey such as KiDS, the SNR from the DM correlations is roughly three times as large and picks up signal at larger scales. This is mainly due to the large f_{sky} in case of the FRBs. Comparing this with Figure 2 we see that, while the noise level is similar for both observables, the smaller area probed by KiDS reduces the overall SNR relative to the FRBs. The green line shows that mainly the small scales add additional signal due to the large correlation between FRBs and lensing. For the state-4 survey, the signal is now dominated by cosmic shear. Especially at high multipoles, only cosmic shear adds any signal.

Reiterating on the previous discussion, we can employ a simple toy model to see whether the SNR ratios obtained are plausible by simply considering individual objects. The SNR for a single sheared lens in cosmic shear is roughly $\text{SNR}_\epsilon \approx 0.03$, assuming that the ellipticity dispersion is roughly 0.3 and the effect of cosmic shear on the ellipticity is roughly a percent. For independent galaxy pairs the total SNR of N such galaxies is $\sqrt{N} \text{SNR}_\epsilon$. Thus, for a SNR of 10^3 one would thus require $\sim 10^9$ galaxies. We can play the same game with FRBs. Let us assume that the variance introduced by the host noise is of the same order as the one introduced by the LSS. This is a conservative estimate, especially at larger z the LSS component will dominate. Therefore the SNR of an individual FRB is unity, independent whether we look at relative or absolute fluctuations. Hence, to achieve an SNR of 100 with $\sim 10^4$ FRBs. Therefore, the SNR we observe in Figure 3 indeed make sense. Since this is a very simple model and the DM scatter of the host galaxy, σ_{host} , is quite uncertain, the total SNR is shown for different noise levels in Figure 4 where both σ_{host} and N_{FRB} are varied while the rest of the survey specifications is kept fixed (i.e. the distribution of FRBs along the line-of-sight). It should also be noted that the host contribution follows rather a log-normal than a Gaussian distribution [71, 72] so σ_{host} should be seen as the corresponding variance to that distribution, which is an accurate description as long as one is considering 2-point correlations only. The fiducial value of $\sigma_{\text{DM}} = 50$ is on the lower end of the plot and it might be considerably larger. On the other hand $N_{\text{FRB}} = 10^4$ is a conservative estimate for the number of FRBs available at later data releases by Euclid or LSST-Rubin at the end of the decade. We would therefore argue that the SNR assumed here is in reasonable reach in that time span. Lastly, we would like to stress that σ_{host} is not the only noise component in the measurement. The total error is given by a sum of cosmic variance

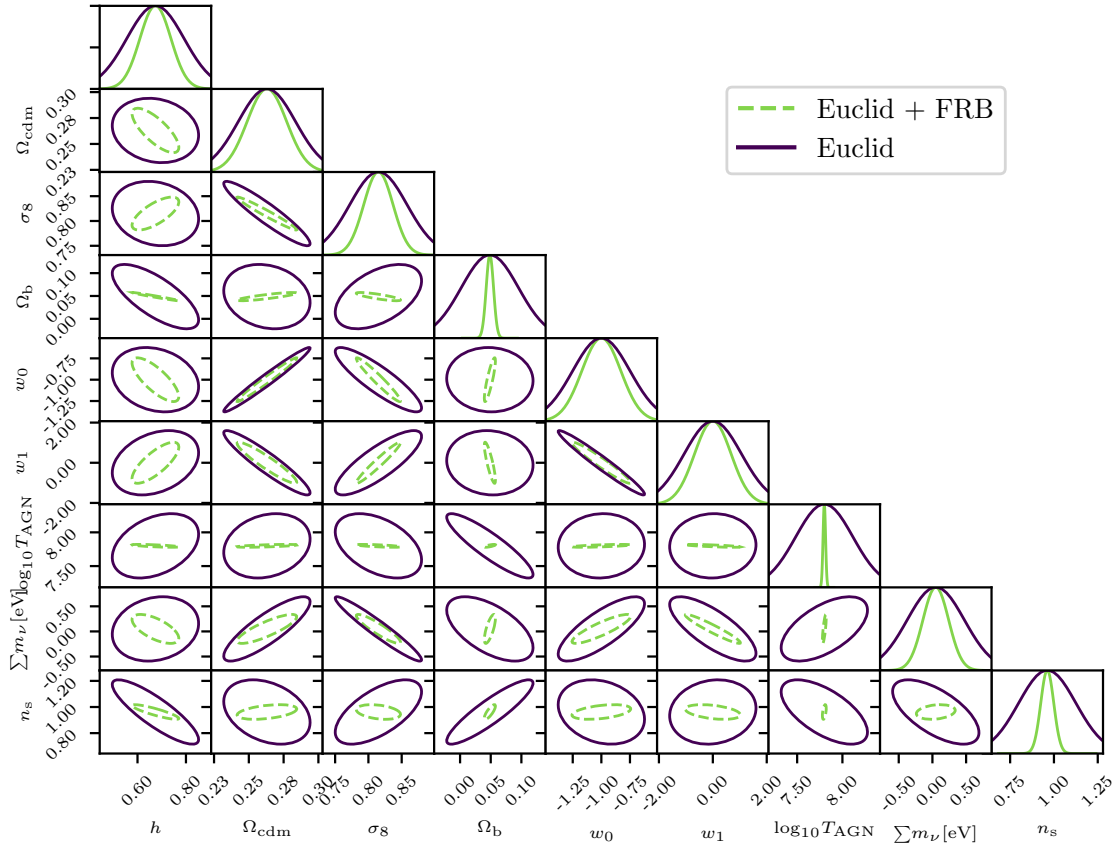


Figure 5. Fisher matrix forecast for Euclid and an FRB survey with $N_{\text{FRB}} = 10^4$ and $\alpha = 3.5$ (compare right panel of Figure 3). Blue contours show the constraints obtainable with, while green contours show the improvement when adding DM correlations. The footprints over which the observables are estimated are assumed to overlap completely. Contours from the FRBs are not shown in this figure, as they are outperformed for most parameters by cosmic shear in this case.

and the host noise contribution. This is exactly taken into account in Equation (2.20), as C_ℓ includes both contributions.

3.2 Cosmological Constraints

We now analyse a set of 9 (5) cosmological and feedback parameters for a stage-4 and a stage-3 survey, respectively, using the setup from the previous section and Table 1. The parameters and the corresponding one dimensional marginal constraints are shown in Table 2. An analogous corner plot is shown in Figure 5 for the case of a stage-4 survey. In general, we distinguish two cases: (i) FRB and cosmic shear auto-correlations separately and (ii) FRB plus cosmic shear, also including the cross-correlation measurements. From Figure 3 we already know that a stage-4 cosmic shear survey outperforms the considered FRB sample by almost a factor of 10 in SNR. It is thus expected that constraints on parameters modifying the amplitude of both spectra simultaneously will be dominated by the cosmic shear measurement. This can be seen clearly in Figure 5, where the amplitude of the power spectrum, σ_8 , is very well constrained by Euclid. Similarly, one finds that the dark energy equation of state parameters w_0 and w_1 assume all the constraining power from the lensing signal as well. This is due to the fact that there is a longer redshift baseline for the cosmic shear survey

and more tomographic information. The FRB sample on the other hand requires a lot of its signal to be put into constraining the total amplitude eq. (2.11), leaving almost no constraining power for the other parameters. Note that this drastically changes by using FRBs with host identification [32, 33]. However, we would like to stress that also unlocalised FRBs still add information to the cosmic shear measurements, even to those parameters typically well constrained by lensing alone. As explained below in more detail, this is caused by the tighter constraints on feedback from DM correlations.

Typical parameters weakly constrained by lensing are the Hubble constant, h and the baryon density Ω_b . Since both enter the amplitude of the DM, it is clear that they can be very well measured with the help of FRBs. The following feature, however, is striking: the constraints on the feedback $\log_{10} T_{\text{AGN}}$ are an order of magnitude better including FRBs compared to cosmic shear alone. The main driver for this effect is that the baryon distribution itself is much more affected by feedback than the total matter distribution, which consists mostly of dark matter, making it more inert to feedback. Similar performance can be expected for more complicated feedback models with more model parameters [65, 67]. In fact, for more free parameters of the feedback, external constraints will become more and more important. Due to the degeneracy between the sum of neutrino masses, $\sum m_\nu$, and the feedback parameter, $\log_{10} T_{\text{AGN}}$, the former will benefit from the increased precision of the latter. Another interesting degeneracy is the primordial slope of the power spectrum, n_s . Fixing this slope is important to connect the clustering strength on small scales with the one measured on larger scales. Cosmic shear alone can only achieve this if the feedback is constrained, showing that FRBs help to break this degeneracy is well. Measuring n_s precisely is very important for the measurement of scale dependent growth on large scales, as is predicted in many theories of modified gravity.

To mimic a more realistic situation, we create a noiseless data vector for the three spectra and estimate the posterior distribution using Markov Chain Monte Carlo (MCMC) sampled by `emcee` [73]. We impose some restrictions to the parameter space by imposing priors on the cosmological parameters. This particularly ensures that the nonlinear power spectrum and electron bias are not extrapolated beyond the range of simulations used to calibrate the model (see also table 1 in [14]). We also summarise the choices for the flat priors in the lower half of Table 2 together with the marginal 68% confidence intervals obtained by cosmic shear alone and cosmic shear combined with FRBs. The trends are very similar, however, we get in general less improvement. The reason for this is that the prior range injects additional information. It can be seen for example that the posteriors for h or Ω_b are prior dominated in the cosmic shear case. Also, the restriction to non-phantom dark energies and no crossing of $w > 0$ reduces the parameter space volume. These effects reduce the gain from adding FRB measurements, since degeneracies are already slightly broken by the prior. Nonetheless, we still find an order of magnitude improvement for the constraints on $\log_{10} T_{\text{AGN}}$ and 50% for the neutrino mass. In Appendix B the effect of the cosmic shear angular power spectrum is shown where it is clear that FRBs (green area) will substantially reduce the prior volume occupied by baryonic feedback models. To underline the importance of this statement it is worth noting that the actual functional form of the power spectrum suppression is not known and the case presented here only describes a very minimal example. For more complex models with more parameters, the addition of additional probes becomes even more important.

Finally, it is worth pointing out that the addition of FRBs also allows cosmic shear to be a more independent probe from the Cosmic Microwave Background (similar to using tSZ or kSZ) as external priors on the baryon density are not required and the parameter can be fitted simultaneously.

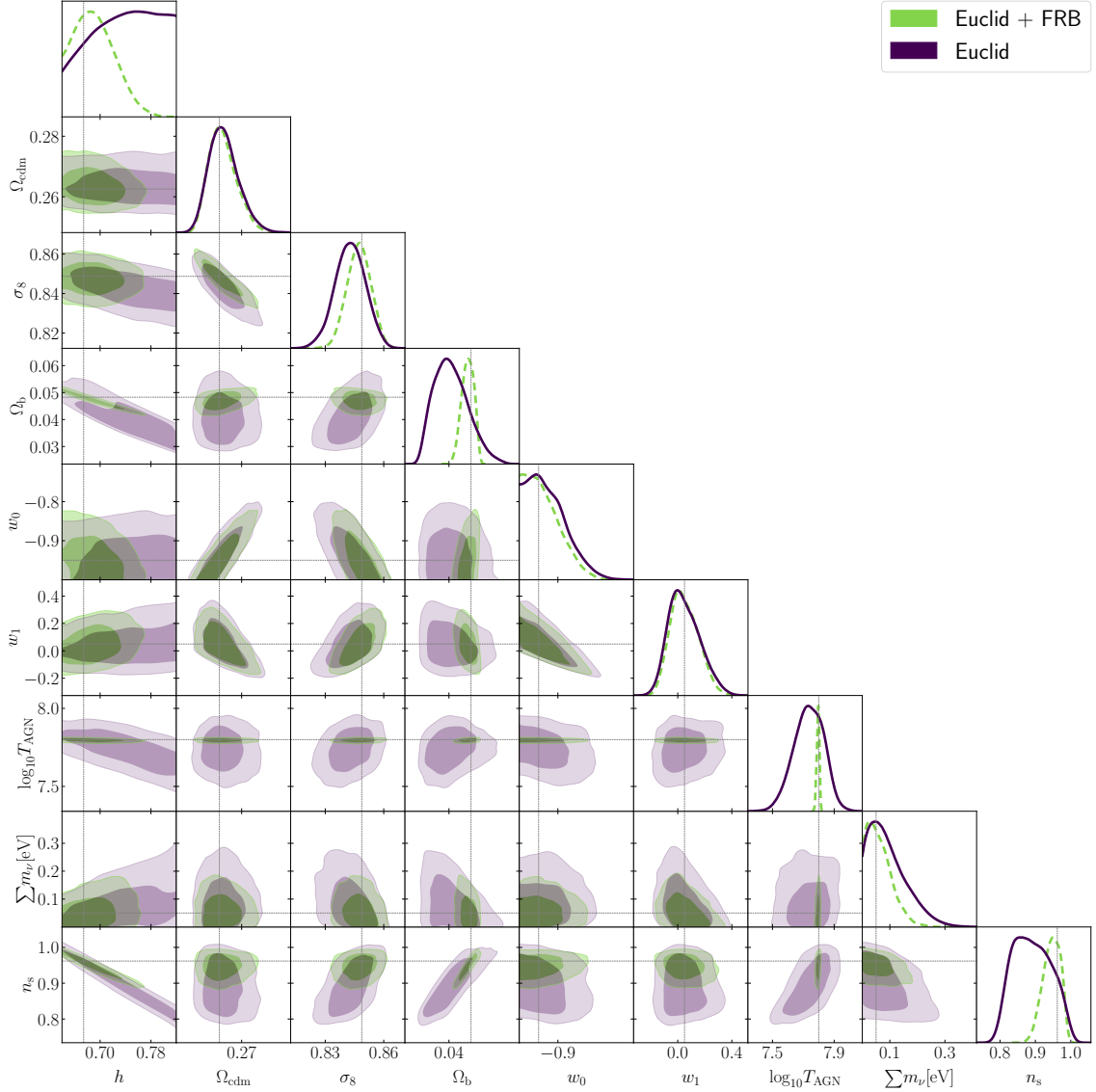


Figure 6. Forecast using a noiseless data vector for Euclid and an FRB survey with $N_{\text{FRB}} = 10^4$ and $\alpha = 3.5$ (compare right panel of Figure 3). Line colours and styles are the same as in Figure 5 with the caveat that the priors from Table 2 are used. The two contours correspond to the standard 68 and 95 % confidence intervals.

4 Conclusion

The ability of future weak lensing surveys to address their key scientific questions, including the search for the mass scale of neutrinos, is largely limited by our understanding of the effect of baryonic physics on the clustering of matter on non-linear scales. While these effects can be measured from simulations, they are vastly different depending on the sub-grid model used. In this work, we investigated an alternative probe of the electron power spectrum, which has been accessible only via the tSZ and kSZ effect so far, the DM angular correlations measured from FRBs. DM correlations are an integrated quantity very similar to cosmic shear, they therefore provides access to very similar scales and can efficiently break degeneracies between cosmological and feedback parameters. Com-

pared to the tSZ and kSZ effects, DM correlations give different weights to different redshifts and scales. While both these probes have, compared to DM correlations, already been detected, the addition of a new probe will achieve a couple of things. Of course it will increase the available signal for LSS measurements. However, more importantly, it provides a completely new look onto the baryon distribution in the Universe, which is independent of the CMB and has completely different systematics. Therefore, while still in its infancy, FRBs can offer an excellent alternative probe. It should also be noticed that FRBs, similar to the kSZ effect, test the electron density and are therefore potentially sensitive to the similar physics. A cross-correlation between the three effects would therefore greatly check the different systematic aspects of the measurements. We used a simple feedback prescription with one parameter to model the matter, electron and matter-electron power spectra and investigated the improvements when cross-correlating a stage-4 cosmic shear survey with the DM from 10^4 FRBs, a number easily achievable within the next years. Our main findings can be summarised as follows:

- i) The DM of FRB observations can improve the constraints on baryonic feedback by an order of magnitude, depending on the SNR of the detection of the DM correlations. Simultaneously, FRBs also help to constrain the Hubble constant and the baryon density. Combining these effects, the constraints on the neutrino mass can be improved by 50 to 100 percent. The SNR used in this work is well in reach within the next decade, considering upcoming observations and dedicated searches for FRBs.
- ii) DM correlations have a different radial weighting function than tSZ measurements, they are therefore sensitive to different redshifts. Furthermore, the observations do not rely directly on the CMB and are hence an entirely different probe at low redshifts with different systematics.

There are a few limiting factors in our analysis. These include a very simple feedback model, Gaussian statistics and the absence of systematic effects. We furthermore did not specify exactly how the $n(z)$ of the FRBs is constructed. A simple way would of course be to observe 10^4 FRBs with host identification. While this is a target for surveys like DSA-2000 or CHORD, one can also think of a subset having a known redshift, which will help to constrain the DM- z relation and therefore allow the construction of an $n(z)$ for the whole sample. We show how this can be in principle done in Appendix D, but save a detailed analysis of this for future work. The scope of this paper was to show that FRBs can be a powerful cosmological probe in particular in conjunction with tracers of the full matter distribution, leveraging the different clustering properties of baryons and dark matter. In the future, we intend to tackle the mentioned limitations by considering a more realistic setup for the inference process.

Acknowledgments

The authors would like to thank two anonymous referees for instructive comments. RR is supported by the European Research Council (Grant No. 770935). SH was supported by the Excellence Cluster ORIGINS which is funded by the Deutsche Forschungsgemeinschaft (DFG, German Research Foundation) under Germany's Excellence Strategy - EXC-2094 - 390783311.

References

- [1] H. Hildebrandt, M. Viola, C. Heymans, S. Joudaki, K. Kuijken, C. Blake et al., *KiDS-450: cosmological parameter constraints from tomographic weak gravitational lensing*, [*MNRAS* **465** \(2017\) 1454](#).
- [2] M. Asgari et al., *KiDS-1000 Cosmology: Cosmic shear constraints and comparison between two point statistics*, [*A&A* **645** \(2021\) A104](#).
- [3] T. M. C. Abbott, F. B. Abdalla, A. Alarcon, J. Aleksić, S. Allam, S. Allen et al., *Dark Energy Survey year 1 results: Cosmological constraints from galaxy clustering and weak lensing*, [*PRD* **98** \(2018\) 043526](#).
- [4] A. Amon, D. Gruen, M. A. Troxel, N. MacCrann, S. Dodelson, A. Choi et al., *Dark Energy Survey Year 3 results: Cosmology from cosmic shear and robustness to data calibration*, [*PRD* **105** \(2022\) 023514](#).
- [5] T. Hamana, M. Shirasaki, S. Miyazaki, C. Hikage, M. Oguri, S. More et al., *Cosmological constraints from cosmic shear two-point correlation functions with HSC survey first-year data*, [*PASJ* **72** \(2020\) 16](#).
- [6] R. Dalal, X. Li, A. Nicola, J. Zuntz, M. A. Strauss, S. Sugiyama et al., *Hyper Suprime-Cam Year 3 results: Cosmology from cosmic shear power spectra*, [*Phys. Rev. D* **108** \(2023\) 123519](#).
- [7] R. S. Somerville and R. Davé, *Physical Models of Galaxy Formation in a Cosmological Framework*, [*Annu. Rev. A&A* **53** \(2015\) 51](#).
- [8] M. Vogelsberger, F. Marinacci, P. Torrey and E. Puchwein, *Cosmological simulations of galaxy formation*, [*NRV* **2** \(2020\) 42](#).
- [9] N. E. Chisari, M. L. A. Richardson, J. Devriendt, Y. Dubois, A. Schneider, A. M. C. Le Brun et al., *The impact of baryons on the matter power spectrum from the Horizon-AGN cosmological hydrodynamical simulation*, [*MNRAS* **480** \(2018\) 3962](#).
- [10] M. P. van Daalen, I. G. McCarthy and J. Schaye, *Exploring the effects of galaxy formation on matter clustering through a library of simulation power spectra*, [*MNRAS* **491** \(2020\) 2424](#).
- [11] F. Villaescusa-Navarro, D. Anglés-Alcázar, S. Genel, D. N. Spergel, R. S. Somerville, R. Dave et al., *The CAMELS Project: Cosmology and Astrophysics with Machine-learning Simulations*, [*APJ* **915** \(2021\) 71](#).
- [12] I. G. McCarthy, J. Schaye, S. Bird and A. M. C. Le Brun, *The BAHAMAS project: calibrated hydrodynamical simulations for large-scale structure cosmology*, [*MNRAS* **465** \(2017\) 2936](#).
- [13] A. J. Mead, T. Tröster, C. Heymans, L. Van Waerbeke and I. G. McCarthy, *A hydrodynamical halo model for weak-lensing cross correlations*, [*A&A* **641** \(2020\) A130](#).
- [14] T. Tröster, A. J. Mead, C. Heymans, Z. Yan, D. Alonso, M. Asgari et al., *Joint constraints on cosmology and the impact of baryon feedback: Combining KiDS-1000 lensing with the thermal Sunyaev-Zeldovich effect from Planck and ACT*, [*AAP* **660** \(2022\) A27](#).
- [15] A. Nicola, F. Villaescusa-Navarro, D. N. Spergel, J. Dunkley, D. Anglés-Alcázar, R. Davé et al., *Breaking baryon-cosmology degeneracy with the electron density power spectrum*, [*JCAP* **2022** \(2022\) 046](#).
- [16] R. A. Sunyaev and Y. B. Zeldovich, *The Observations of Relic Radiation as a Test of the Nature of X-Ray Radiation from the Clusters of Galaxies*, *Comments on ASP* **4** (1972) 173.
- [17] R. A. Sunyaev and I. B. Zeldovich, *Microwave background radiation as a probe of the contemporary structure and history of the universe*, [*ARAA* **18** \(1980\) 537](#).
- [18] N. Hand, G. E. Addison, E. Aubourg, N. Battaglia, E. S. Battistelli, D. Bizyaev et al., *Evidence of Galaxy Cluster Motions with the Kinematic Sunyaev-Zel'dovich Effect*, [*PRL* **109** \(2012\) 041101](#).
- [19] E. Schaan, S. Ferraro, M. Vargas-Magaña, K. M. Smith, S. Ho, S. Aiola et al., *Evidence for the kinematic sunyaev-zel'dovich effect with the atacama cosmology telescope and velocity reconstruction from the baryon oscillation spectroscopic survey*, [*PRD* **93** \(2016\) 082002](#).

- [20] P. A. R. Ade, N. Aghanim, M. Arnaud, M. Ashdown, E. Aubourg, J. Aumont et al., *Planck intermediate results. XXXVII. Evidence of unbound gas from the kinetic Sunyaev-Zeldovich effect*, [*AAP* **586** \(2016\) A140](#).
- [21] B. Soergel, S. Flender, K. T. Story, L. Bleem, T. Giannantonio, G. Efstathiou et al., *Detection of the kinematic Sunyaev-Zel'dovich effect with DES Year 1 and SPT*, [*MNRAS* **461** \(2016\) 3172](#).
- [22] E. Schaan, S. Ferraro, S. Amodeo, N. Battaglia, S. Aiola, J. E. Austermann et al., *Atacama cosmology telescope: Combined kinematic and thermal sunyaev-zel'dovich measurements from boss cmass and lowz halos*, [*PRD* **103** \(2021\) 063513](#).
- [23] S. Amodeo, N. Battaglia, E. Schaan, S. Ferraro, E. Moser, S. Aiola et al., *Atacama Cosmology Telescope: Modeling the gas thermodynamics in BOSS CMASS galaxies from kinematic and thermal Sunyaev-Zel'dovich measurements*, [*PRD* **103** \(2021\) 063514](#).
- [24] B. Hadzhiyska, S. Ferraro, B. Ried Guachalla, E. Schaan, J. Aguilar, N. Battaglia et al., *Evidence for large baryonic feedback at low and intermediate redshifts from kinematic Sunyaev-Zel'dovich observations with ACT and DESI photometric galaxies*, [*arXiv e-prints* \(2024\) arXiv:2407.07152 \[2407.07152\]](#).
- [25] I. G. McCarthy, A. Amon, J. Schaye, E. Schaan, R. E. Angulo, J. Salcido et al., *FLAMINGO: combining kinetic SZ effect and galaxy-galaxy lensing measurements to gauge the impact of feedback on large-scale structure*, [*arXiv e-prints* \(2024\) arXiv:2410.19905 \[2410.19905\]](#).
- [26] D. Thornton, B. Stappers, M. Bailes, B. Barsdell, S. Bates, N. D. R. Bhat et al., *A Population of Fast Radio Bursts at Cosmological Distances*, [*Science* **341** \(2013\) 53](#).
- [27] E. Petroff, M. Bailes, E. D. Barr, B. R. Barsdell, N. D. R. Bhat, F. Bian et al., *A real-time fast radio burst: polarization detection and multiwavelength follow-up*, [*MNRAS* **447** \(2015\) 246](#).
- [28] L. Connor, J. Sievers and U.-L. Pen, *Non-cosmological FRBs from young supernova remnant pulsars*, [*MNRAS* **458** \(2016\) L19](#).
- [29] D. J. Champion, E. Petroff, M. Kramer, M. J. Keith, M. Bailes, E. D. Barr et al., *Five new fast radio bursts from the HTRU high-latitude survey at Parkes: first evidence for two-component bursts*, [*MNRAS* **460** \(2016\) L30](#).
- [30] S. Chatterjee, C. J. Law, R. S. Wharton, S. Burke-Spolaor, J. W. T. Hessels, G. C. Bower et al., *A direct localization of a fast radio burst and its host*, [*Nature* **541** \(2017\) 58](#).
- [31] B. Zhou, X. Li, T. Wang, Y.-Z. Fan and D.-M. Wei, *Fast radio bursts as a cosmic probe?*, [*PRD* **89** \(2014\) 107303](#).
- [32] A. Walters, A. Weltman, B. M. Gaensler, Y.-Z. Ma and A. Witzemann, *Future Cosmological Constraints From Fast Radio Bursts*, [*APJ* **856** \(2018\) 65](#).
- [33] S. Hagstotz, R. Reischke and R. Lilow, *A new measurement of the Hubble constant using fast radio bursts*, [*MNRAS* **511** \(2022\) 662](#).
- [34] J.-P. Macquart, J. X. Prochaska, M. McQuinn, K. W. Bannister, S. Bhandari, C. K. Day et al., *A census of baryons in the Universe from localized fast radio bursts*, [*Nature* **581** \(2020\) 391](#).
- [35] Q. Wu, G.-Q. Zhang and F.-Y. Wang, *An 8 per cent determination of the Hubble constant from localized fast radio bursts*, [*MNRAS* **515** \(2022\) L1](#).
- [36] C. W. James, E. M. Ghosh, J. X. Prochaska, K. W. Bannister, S. Bhandari, C. K. Day et al., *A measurement of Hubble's Constant using Fast Radio Bursts*, [*MNRAS* **516** \(2022\) 4862](#).
- [37] R. Reischke and S. Hagstotz, *Consistent constraints on the equivalence principle from localized fast radio bursts*, [*MNRAS* **523** \(2023\) 6264](#).
- [38] R. Reischke and S. Hagstotz, *Cosmological covariance of fast radio burst dispersions*, [*MNRAS* **524** \(2023\) 2237](#).

- [39] K. W. Masui and K. Sigurdson, *Dispersion Distance and the Matter Distribution of the Universe in Dispersion Space*, [*PRL* **115** \(2015\) 121301](#).
- [40] M. Shirasaki, K. Kashiyama and N. Yoshida, *Large-scale clustering as a probe of the origin and the host environment of fast radio bursts*, [*PRD* **95** \(2017\) 083012](#).
- [41] M. Raffei-Ravandi, K. M. Smith, D. Li, K. W. Masui, A. Josephy, M. Dobbs et al., *CHIME/FRB Catalog 1 Results: Statistical Cross-correlations with Large-scale Structure*, [*ApJ* **922** \(2021\) 42](#).
- [42] M. Bhattacharya, P. Kumar and E. V. Linder, *Fast radio burst dispersion measure distribution as a probe of helium reionization*, [*PRD* **103** \(2021\) 103526](#).
- [43] R. Takahashi, K. Ioka, A. Mori and K. Funahashi, *Statistical modelling of the cosmological dispersion measure*, [*MNRAS* **502** \(2021\) 2615](#).
- [44] R. Reischke, S. Hagstotz and R. Lilow, *Probing primordial non-Gaussianity with Fast Radio Bursts*, [*PRD* **103** \(2021\) 023517](#).
- [45] R. Reischke, S. Hagstotz and R. Lilow, *Consistent equivalence principle tests with fast radio bursts*, [*MNRAS* **512** \(2022\) 285](#).
- [46] S. Johnston, R. Taylor, M. Bailes, N. Bartel, C. Baugh, M. Bietenholz et al., *Science with ASKAP - the Australian Square Kilometre Array Pathfinder*, [*Exp Astron* **22** \(2008\) 151](#).
- [47] D. J. Bacon, R. A. Battye, P. Bull, S. Camera, P. G. Ferreira, I. Harrison et al., *Cosmology with Phase 1 of the Square Kilometre Array Red Book 2018: Technical specifications and performance forecasts*, [*PASA* **37** \(2020\) e007](#).
- [48] M. Caleb, C. Flynn, M. Bailes, E. D. Barr, T. Bateman, S. Bhandari et al., *Fast Radio Transient searches with UTMOST at 843 MHz*, [*MNRAS* **458** \(2016\) 718](#).
- [49] L. B. Newburgh, K. Bandura, M. A. Bucher, T. C. Chang, H. C. Chiang, J. F. Cliche et al., *HIRAX: a probe of dark energy and radio transients*, in *Ground-based and Airborne Telescopes VI* (H. J. Hall, R. Gilmozzi and H. K. Marshall, eds.), vol. 9906 of *Society of Photo-Optical Instrumentation Engineers (SPIE) Conference Series*, p. 99065X, Aug., 2016, [DOI](#).
- [50] G. Hallinan, V. Ravi, S. Weinreb, J. Kocz, Y. Huang, D. P. Woody et al., *The DSA-2000 — A Radio Survey Camera*, in *Bulletin of the AAS*, vol. 51, p. 255, Sept., 2019, [DOI](#).
- [51] K. Vanderlinde, A. Liu, B. Gaensler, D. Bond, G. Hinshaw, C. Ng et al., *The Canadian Hydrogen Observatory and Radio-transient Detector (CHORD)*, in *Canadian Long Range Plan for Astronomy and Astrophysics White Papers*, vol. 2020, p. 28, Oct., 2019, [DOI](#).
- [52] J. M. Yao, R. N. Manchester and N. Wang, *A New Electron-density Model for Estimation of Pulsar and FRB Distances*, [*APJ* **835** \(2017\) 29](#).
- [53] D. N. Limber, *The Analysis of Counts of the Extragalactic Nebulae in Terms of a Fluctuating Density Field. II.*, [*ApJ* **119** \(1954\) 655](#).
- [54] M. Loverde and N. Afshordi, *Extended Limber approximation*, [*Phys. Rev. D* **78** \(2008\) 123506](#).
- [55] C. D. Leonard, T. Ferreira, X. Fang, R. Reischke, N. Schoeneberg, T. Tröster et al., *The N5K Challenge: Non-Limber Integration for LSST Cosmology*, [*The Open Journal of Astrophysics* **6** \(2023\) 8](#).
- [56] A. J. Mead, J. A. Peacock, C. Heymans, S. Joudaki and A. F. Heavens, *An accurate halo model for fitting non-linear cosmological power spectra and baryonic feedback models*, [*MNRAS* **454** \(2015\) 1958](#).
- [57] A. Blanchard, S. Camera, C. Carbone, V. F. Cardone, S. Casas, S. Clesse et al., *Euclid preparation. VII. Forecast validation for Euclid cosmological probes*, [*AAP* **642** \(2020\) A191 \[1910.09273\]](#).
- [58] B. Joachimi, C. A. Lin, M. Asgari, T. Tröster, C. Heymans, H. Hildebrandt et al., *KiDS-1000 methodology: Modelling and inference for joint weak gravitational lensing and spectroscopic galaxy clustering analysis*, [*AAP* **646** \(2021\) A129](#).

- [59] E. Platts, J. X. Prochaska and C. J. Law, *A Data-driven Technique Using Millisecond Transients to Measure the Milky Way Halo*, [*APJ* **895** \(2020\) L49](#).
- [60] A. A. Meiksin, *The physics of the intergalactic medium*, [*RoMP* **81** \(2009\) 1405](#).
- [61] G. D. Becker, J. S. Bolton, M. G. Haehnelt and W. L. W. Sargent, *Detection of extended He II reionization in the temperature evolution of the intergalactic medium*, [*MNRAS* **410** \(2011\) 1096](#).
- [62] J. M. Shull, B. D. Smith and C. W. Danforth, *The Baryon Census in a Multiphase Intergalactic Medium: 30% of the Baryons May Still be Missing*, [*APJ* **759** \(2012\) 23](#).
- [63] C. W. James, J. X. Prochaska, J.-P. Macquart, F. North-Hickey, K. W. Bannister and A. Dunning, *The z -DM distribution of fast radio bursts*, [*MNRAS* **509** \(2021\) 4775](#).
- [64] A. M. C. Le Brun, I. G. McCarthy, J. Schaye and T. J. Ponman, *Towards a realistic population of simulated galaxy groups and clusters*, [*MNRAS* **441** \(2014\) 1270](#).
- [65] R. E. Angulo, M. Zennaro, S. Contreras, G. Aricò, M. Pellejero-Ibañez and J. Stücker, *The BACCO simulation project: exploiting the full power of large-scale structure for cosmology*, [*MNRAS* **507** \(2021\) 5869](#).
- [66] G. Aricò, R. E. Angulo, C. Hernández-Monteagudo, S. Contreras and M. Zennaro, *Simultaneous modelling of matter power spectrum and bispectrum in the presence of baryons*, [*MNRAS* **503** \(2021\) 3596](#).
- [67] G. Aricò, R. E. Angulo, S. Contreras, L. Ondaro-Mallea, M. Pellejero-Ibañez and M. Zennaro, *The BACCO simulation project: a baryonification emulator with neural networks*, [*MNRAS* **506** \(2021\) 4070](#).
- [68] M. Tegmark, A. N. Taylor and A. F. Heavens, *Karhunen-Loève Eigenvalue Problems in Cosmology: How Should We Tackle Large Data Sets?*, [*ApJ* **480** \(1997\) 22](#).
- [69] R. Reischke, *Propagating photo- z uncertainties: a functional derivative approach*, [*MNRAS* **530** \(2024\) 4412](#).
- [70] H. Hildebrandt, J. L. van den Busch, A. H. Wright, C. Blake, B. Joachimi, K. Kuijken et al., *KiDS-1000 catalogue: Redshift distributions and their calibration*, [*AAP* **647** \(2021\) A124](#).
- [71] Z. J. Zhang, K. Yan, C. M. Li, G. Q. Zhang and F. Y. Wang, *Intergalactic medium dispersion measures of fast radio bursts estimated from IllustrisTNG simulation and their cosmological applications*, [*APJ* **906** \(2021\) 49](#).
- [72] J.-F. Mo, W. Zhu, Y. Wang, L. Tang and L.-L. Feng, *The dispersion measure of Fast Radio Bursts host galaxies: estimation from cosmological simulations*, [*MNRAS* **518** \(2022\) 539](#).
- [73] D. Foreman-Mackey, D. W. Hogg, D. Lang and J. Goodman, *emcee: The MCMC Hammer*, [*PASP* **125** \(2013\) 306](#).
- [74] C. Heymans, T. Tröster, M. Asgari, C. Blake, H. Hildebrandt, B. Joachimi et al., *KiDS-1000 Cosmology: Multi-probe weak gravitational lensing and spectroscopic galaxy clustering constraints*, [*AAP* **646** \(2021\) A140](#).
- [75] N. Aghanim, Y. Akrami, M. Ashdown, J. Aumont, C. Baccigalupi, M. Ballardini et al., *Planck 2018 results. VI. Cosmological parameters*, [*A&A* **641** \(2020\) A6](#).

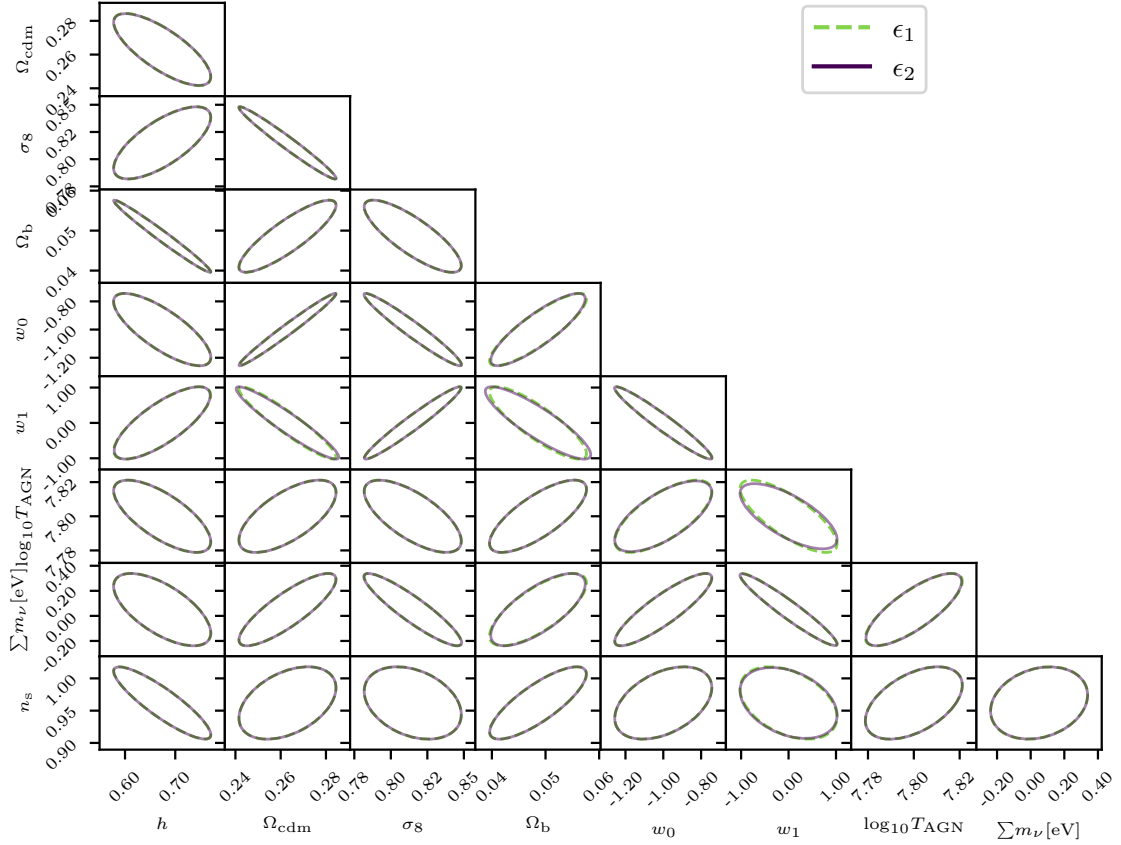


Figure 7. Same as Figure 5 but with varying step size for the numerical derivative. In particular, we choose $\epsilon_3 = 10^{-3}$ and $\epsilon_1 = 10^{-2}$ for the green and dark violet lines, respectively. The fiducial case in Figure 5 assumes $\epsilon_1 = 5 \times 10^{-3}$.

A Stability of the Fisher matrix

To ensure the stability of the Fisher matrix, we vary the step size with which we evaluate the derivative. This exercise is shown in Figure 7 for two different choices for ϵ . In particular, we take the central form of the finite difference and vary the parameters by

$$\delta\theta_{i\pm} = \begin{cases} \theta_{i,0}(1 \pm \epsilon) & \text{if } \theta_{i,0} \neq 0 \\ \pm\epsilon & \text{else} \end{cases}, \quad (\text{A.1})$$

where $\theta_{i,0}$ is the parameter's fiducial value.

B Effects of feedback on angular power spectra

In Figure 8 we show the effect of adding FRBs to a cosmic shear measurement. The coloured lines show different feedback models quantified by the $\log_{10} T_{\text{AGN}}$ parameter and the expected Euclid statistical error bars on the power spectrum. It is clear that cosmic shear alone would need to put a significant fraction of its signal into constraining the baryonic feedback model (i.e. $\log_{10} T_{\text{AGN}}$). However, adding FRBs reduces the possible range of feedback models to the green band, greatly

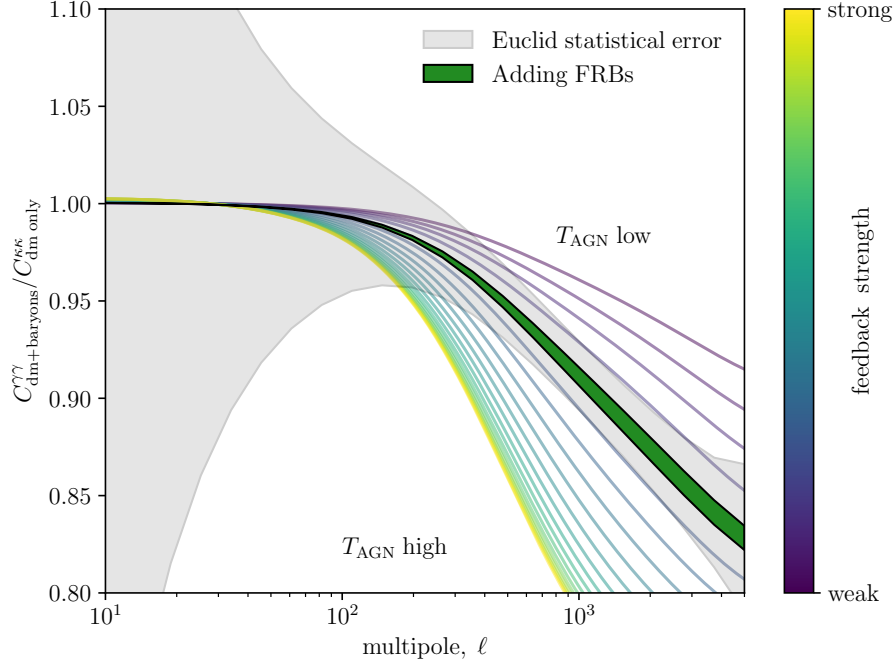


Figure 8. Effect of baryonic feedback on a typical angular power spectra of cosmic shear. In particular we show the ratio of the power spectrum with (dark matter plus baryons) and without (dark matter only) feedback. The colour bar shows the strength of feedback that scales with T_{AGN} , giving an indication of the possible prior range of angular power spectra. The grey band shows Euclid-like error bars around a reference feedback model with $\log_{10} T_{\text{AGN}} = 7.6$. The green band shows by how much the feedback model will be constrained when adding FRBs to cosmic shear.

reducing the uncertainty and allowing cosmic shear to put more signal into other cosmological parameters.

C Influence of redshift uncertainty on the inference

Here we investigate the influence of an unknown mean redshift of the FRB sample and its redshift distribution n_{FRB} . To this end, we shift the mean by an arbitrary number, δz , and marginalise these new free parameters. The result is shown in Figure 9 where the case with known redshifts is shown in black and with an unknown mean of the distribution in dashed (red). Clearly, the influence of the marginalisation of the shift is minimal. The reason for this is that the redshift distribution can be self-calibrated very well because of the overlap with a calibrated redshift distribution of the cosmic shear sample. Although this is a very simplified analysis, it shows that it is in principle possible to use a good fraction of FRBs without host identification for cross-correlation studies, as presented in this work. Another reason why the influence of the unknown redshifts is small is that the effect investigated here has a complicated redshift and scale dependence, so the model can tell these two effects apart.

D Noise increase due to redshift uncertainty

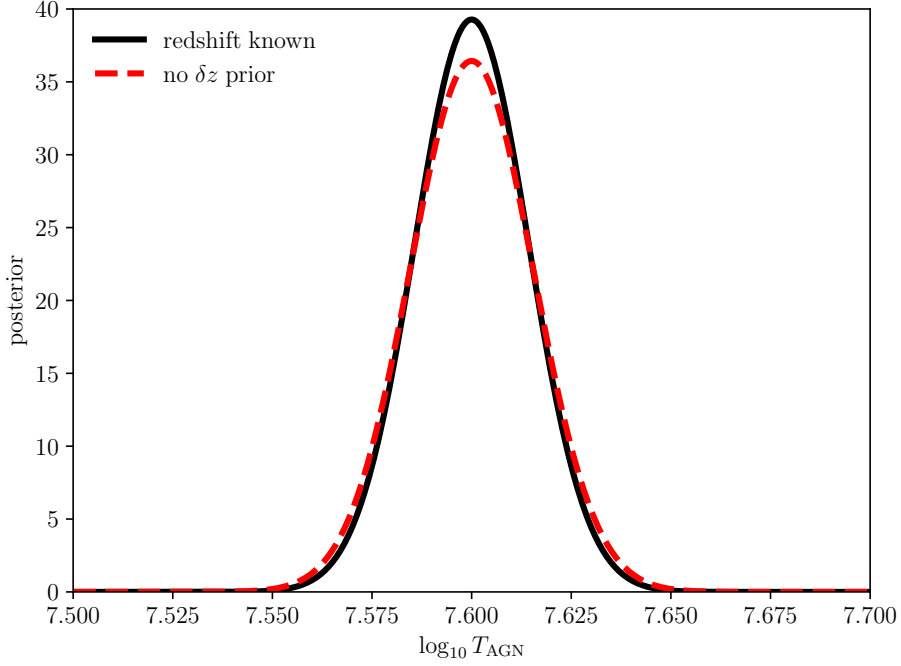


Figure 9. Influence of marginalising over the redshift shift parameter δz on the 1D marginal constraints of the feedback parameter $\log_{10} T_{\text{AGN}}$. The black curve assumes a Dirac delta prior centred at $\delta z = 0$, i.e. perfectly known redshifts, while the red-dashed line assumes no prior information.

While the previous section showed that the An additional effect arises due to the unknown redshift distribution of the FRBs can be auto-calibrated by the known redshift distribution of the cosmic shear sample, an additional effect arises. In Equation (2.27), the residual redshifts of the FRB sample introduce a redshift scatter and hence a scatter in the DM, acting as an additional noise term in the covariance. Therefore, instead of the replacement in Equation (2.17), we write:

$$C^{\mathcal{D}\mathcal{D}}(\ell) \rightarrow C^{\mathcal{D}\mathcal{D}}(\ell) + \frac{\sigma_{\text{host}}^2}{\bar{n}} + \frac{\sigma_z^2}{\bar{n}}. \quad (\text{D.1})$$

The magnitude of σ_z^2 hinges on our ability to exploit the DM-redshift relation in Equation (2.25). To estimate this effect, we assume that we are given N_{FRB} FRBs from which a fraction, f^z , has measured redshifts. Those $N_{\text{FRB}}^z = f^z N_{\text{FRB}}$ are then used to fit a cosmological model to the DM- z relation. We sample N_{FRB}^z from the redshift distribution and collect them in the vectors $\mathbf{z} = (z_1, \dots, z_n)^T$ and

$$\boldsymbol{\mu} = \left(\text{DM}_{\text{LSS}}(z_1) + \frac{\text{DM}_{\text{host},0}}{1+z_1}, \dots, \text{DM}_{\text{LSS}}(z_n) + \frac{\text{DM}_{\text{host},0}}{1+z_n} \right)^T, \quad (\text{D.2})$$

with $n = N_{\text{FRB}}^z$ and the mean DM given by:

$$\langle \text{DM}_{\text{LSS}}(\hat{\mathbf{x}}, \mathbf{z}) \rangle \equiv \text{DM}_{\text{LSS}}(\mathbf{z}) = \mathcal{A} \int_0^z dz' \frac{1+z'}{E(z')} F(z'). \quad (\text{D.3})$$

For simplicity, we assume a Gaussian likelihood and calculate the corresponding Fisher matrix:

$$F_{\alpha\beta} = \partial_\alpha \boldsymbol{\mu}^T \mathbf{C}^{-1} \partial_\beta \boldsymbol{\mu}, \quad (\text{D.4})$$

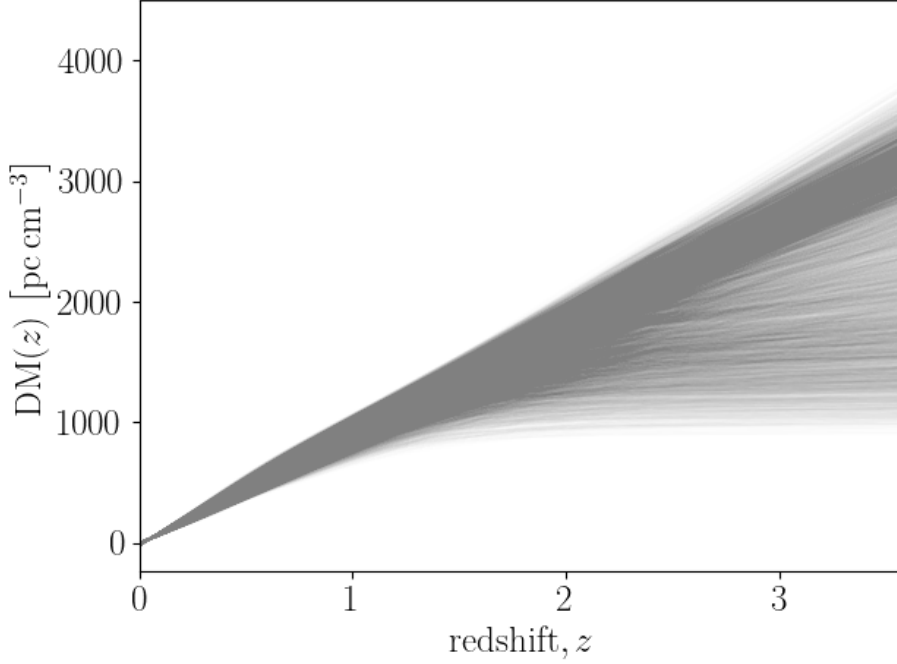


Figure 10. Model predictions for the DM-redshift relation of the 68 % confidence interval on the using $N_{\text{FRB}}^z = 100$ FRBs with redshift information. In this figure, all parameters responsible for the background evolution in Table 2 are fitted, and the host contribution, $\text{DM}_{\text{host},0}$, is marginalised over. Note that the scatter between different redshifts is highly correlated, due to the constraints on the functional form by the model.

where $\boldsymbol{\mu}$ is the vector containing all N_{FRB}^z of $\text{DM}_{\text{LSS}}(z)$ and the components of the covariance is given by:

$$C_{ij} = C_{\text{LSS},ij} + \sigma_{\text{MW}}^2 \delta_{ij}^{\text{K}} + \sigma_{\text{host}}^2(z_i) \delta_{ij}^{\text{K}}. \quad (\text{D.5})$$

Here $C_{\text{LSS},ij}$ is calculated via the formalism discussed in [38] and $\sigma_{\text{MW}} = 30 \text{ pc cm}^{-3}$ is the residual uncertainty from the Milky Way contribution. Additionally, we will assume the prior information we use in Table 2 for the MCMC case, mimicing typical choices in stage-3 weak lensing surveys (see e.g. Table B.1 in [74]).

By sampling from the resulting posterior distribution, model predictions are produced. The corresponding DM-redshift relations are plotted in Figure 10 using $N_{\text{FRB}}^z = 100$ for parameters drawn from the 68 % confidence interval. We use the scatter of this relation as an estimate for $\sigma_z^2(z)$, such that $\sigma_z^2 = \int n_{\text{FRB}}(z) \sigma_z^2(z)$. In Figure 11 on the left, the effective contribution to the error in the redshift estimation is shown as solid lines for increasing number of FRBs with redshift information. The dashed lines assume a prior using the CMB [75]. In the right panel, we show how this additional noise term influences the cumulative SNR relative to the fiducial analysis with the same colour-coding and linestyles. For example, 100 FRBs with host identification, will and 9900 unknown, will reduce the overall SNR of our measurement by 70 percent. As soon as external data is added, however, the noise contribution from the initial redshift uncertainty is negligible for the overall SNR. To be conservative and for simplicity, we have assumed, that all FRBs share the same redshift uncertainty (also the ones with a known redshift). Furthermore, we have assumed that the fluctuations at different redshifts are all independent, thus placing a ceiling on the redshift uncertainty.

In this way, we have utilised the homogeneous component of the localised sub-sample to mea-

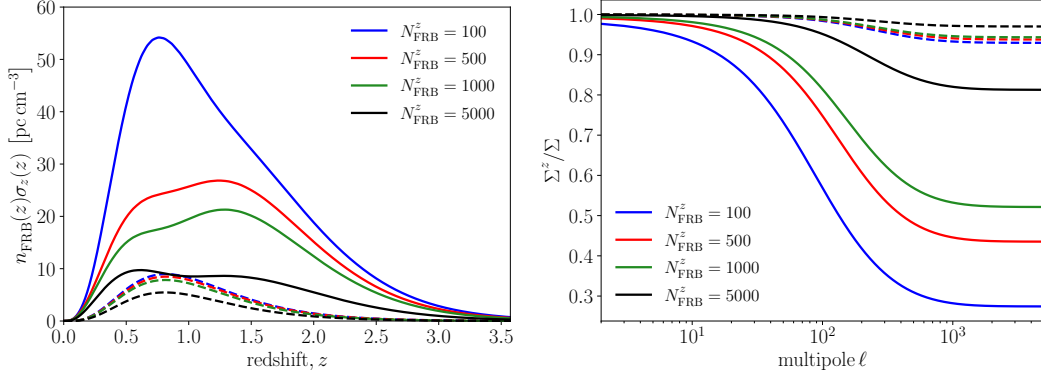


Figure 11. *Left:* Contribution to the redshift uncertainty for unlocalised FRBs as deduced from the inference of $\text{DM}_{\text{LSS}}(z)$ in Figure 10. The uncertainty is weighted by the fiducial redshift distribution. Solid lines only use N_{FRB}^z to calibrate $\text{DM}_{\text{LSS}}(z)$, while dashed lines use CMB information. *Right:* Corresponding cumulative SNR loss relative to the fiducial (compare with Figure 3 and Figure 4).

sure the DM-redshift relation and therefore provide noisy estimates of the redshift. This is then followed by using the full FRB sample to calculate angular clustering of the DM. Here we neglected the cross-correlation between these two procedures which is justifiable since it is small compared to the respective auto-correlations as it is only sourced by a bispectrum:

$$\begin{aligned} \text{cov} [\text{DM}_{\text{LSS}}(\hat{\mathbf{x}}_1, z_1), \mathcal{D}(\hat{\mathbf{x}}_2)\mathcal{D}(\hat{\mathbf{x}}_3)] &\equiv \langle \text{DM}_{\text{LSS}}(\hat{\mathbf{x}}_1, z), \mathcal{D}(\hat{\mathbf{x}}_2)\mathcal{D}(\hat{\mathbf{x}}_3) \rangle - \text{DM}_{\text{LSS}}(z) \langle \mathcal{D}(\hat{\mathbf{x}}_2)\mathcal{D}(\hat{\mathbf{x}}_3) \rangle \\ &= \mathcal{A} \int_0^z dz' \frac{1+z'}{E(z')} F(z') \int_0^{\chi_H} d\chi W_{\mathcal{D}}(\chi) \int_0^{\chi_H} d\chi' W_{\mathcal{D}}(\chi') \langle \delta_e(\hat{\mathbf{x}}_3, z(\chi)) \delta_e(\hat{\mathbf{x}}_2, z(\chi')) \delta_e(\hat{\mathbf{x}}_1, z') \rangle. \end{aligned} \quad (\text{D.6})$$

This discussion, together with Appendix C shows that there is the potential to self-calibrate the redshift distribution of FRBs, even if only a subset of FRBs are localised.